(4)

TECHNICAL REPORT BRL-TR-2962

BRL

1938 – Serving the Army for Fifty Years – 1988

AD-A202 412

NUMERICAL COMPUTATIONS OF TRANSONIC CRITICAL AERODYNAMIC BEHAVIOR

JUBARAJ SAHU

DECEMBER 1988

DTIC
ELECTE
JAN 1 2 1989
S D
H

U.S. ARMY LABORATORY COMMAND

BALLISTIC RESEARCH LABORATORY

ABERDEEN PROVING GROUND, MARYLAND

89   1 12   022

REPORT DOCUMENTATION PAGE		Form Approved OMB No. 0704-0188

1a. REPORT SECURITY CLASSIFICATION UNCLASSIFIED	1b. RESTRICTIVE MARKINGS
2a. SECURITY CLASSIFICATION AUTHORITY	3. DISTRIBUTION/AVAILABILITY OF REPORT Approved for public release, distribution unlimited.
2b. DECLASSIFICATION/DOWNGRADING SCHEDULE	
4. PERFORMING ORGANIZATION REPORT NUMBER(S) BRL-TR-2962	5. MONITORING ORGANIZATION REPORT NUMBER(S)

6a. NAME OF PERFORMING ORGANIZATION U.S. Army Ballistic Research Laboratory	6b. OFFICE SYMBOL (If applicable) SLCBR-LF	7a. NAME OF MONITORING ORGANIZATION
6c. ADDRESS (City, State, and ZIP Code) Aberdeen Proving Ground, Maryland 21005-5066		7b. ADDRESS (City, State, and ZIP Code)
8a. NAME OF FUNDING/SPONSORING ORGANIZATION	8b. OFFICE SYMBOL (If applicable)	9. PROCUREMENT INSTRUMENT IDENTIFICATION NUMBER

8c. ADDRESS (City, State, and ZIP Code)	10. SOURCE OF FUNDING NUMBERS			
	PROGRAM ELEMENT NO. 61102A	PROJECT NO. 1L161102AH43	TASK NO. 00	WORK UNIT ACCESSION NO. 001 AJ

11. TITLE (Include Security Classification)

NUMERICAL COMPUTATIONS OF TRANSONIC CRITICAL AERODYNAMIC BEHAVIOR

12. PERSONAL AUTHOR(S)
JUBARAJ SAHU

13a. TYPE OF REPORT Technical Report	13b. TIME COVERED FROM _____ TO _____	14. DATE OF REPORT (Year, Month, Day) September 1988	15. PAGE COUNT 30

16. SUPPLEMENTARY NOTATION

17. COSATI CODES			18. SUBJECT TERMS (Continue on reverse if necessary and identify by block number)
FIELD	GROUP	SUB-GROUP	Critical Aerodynamic Behavior; Transonic Flows
01	01		Implicit Scheme, Flux-split Upwind Algorithm, Navier/Stokes Numerical Computations, Composite Grid Partitioning.

19. ABSTRACT (Continue on reverse if necessary and identify by block number)

The determination of aerodynamic coefficients by shell designers is a critical step in the development of any new projectile design. Of particular interest is the determination of the aerodynamic coefficients at transonic speeds. It is in this speed regime that the critical aerodynamic behavior occurs and a rapid change in the aerodynamic coefficients is observed. Three-dimensional transonic flow field computations over projectiles have been made using an implicit, approximately factored, partially flux-split algorithm. A composite grid scheme has been used to provide the increased grid resolution needed for accurate numerical simulation of three-dimensional transonic flows. Details of the asymmetrically located shockwaves on the projectiles have been determined. Computed surface pressures have been compared with experimental data and are found to be in good agreement. The pitching moment coefficient, determined from the computed flow fields, shows the critical aerodynamic behavior observed in free flights.

20. DISTRIBUTION/AVAILABILITY OF ABSTRACT ☒ UNCLASSIFIED/UNLIMITED ☐ SAME AS RPT ☐ DTIC USERS	21. ABSTRACT SECURITY CLASSIFICATION UNCLASSIFIED	
22a. NAME OF RESPONSIBLE INDIVIDUAL Jubaraj Sahu	22b. TELEPHONE (Include Area Code) (301) 278-3707	22c. OFFICE SYMBOL SLCBR-LF-C

DD Form 1473, JUN 86   Previous editions are obsolete.   SECURITY CLASSIFICATION OF THIS PAGE

TABLE OF CONTENTS

Accession For

A-1

iii

LIST OF FIGURES

I. INTRODUCTION

The flight of projectiles covers a wide range of speeds. The accurate prediction of projectile aerodynamics at these speeds is of significant importance in the early design stage of a projectile. The critical aerodynamic behavior occurs in the transonic speed regime, $0.9 < M < 1.1$ where the aerodynamic coefficients have been found to change by as much as 100%. Of particular interest is the determination of the pitching moment coefficient since it is used to determine the static stability of the projectile. The critical behavior in this case is usually characterized by a rapid increase in the coefficient followed by a sharp drop. This rapid change in the pitching moment coefficient can be attributed in part to the complex flow structure and in particular, to the asymmetrically located shock waves which exist on projectiles flying at transonic speeds at angle of attack. Computations of three-dimensional flowfields at transonic speeds are thus needed to predict the critical aerodynamic behavior.

In recent years a considerable research effort has been focused on the development of modern predictive capabilities for determining projectile aerodynamics. Numerical capabilities have been developed primarily using Navier-Stokes[1-5] computational techniques and used to compute flow over slender bodies of revolution at transonic speeds. Flowfield computations have included both axisymmetric[4] and three-dimensional situations.[1,2,3,5] Initial computations[1-3] did not include the wake or base region of a projectile and, thus, ignored the upstream effect of the base region flow on the afterbody. An axisymmetric base flow code[4] was then developed to compute the entire projectile flowfield including the base region. The base flow code used a flowfield segmentation procedure which preserved the sharp base corner. This technique was later extended[5] into three dimensions to calculate the pitch plane aerodynamics at transonic speeds. Due to lack of computer resources, only one solution was obtained and reported in Reference 5. In addition, the calculations in References 1, 2, 3 and 5 generally did not have sufficient grid resolution due to the lack of adequate computer resources. The availability of supercomputers such as the Cray X-MP/48 with a 128 million word solid state disk device (SSD) and the Cray 2 allows for the increased grid resolution which is needed for accurate computations of three-dimensional transonic flows.[6]

The numerical scheme plays an equally important role for accurate predictions of transonic flows. All the calculations in Reference 1-5 were made using the compressible, thin-layer Navier-Stokes equations which were solved using the implicit Beam and Warming central finite difference scheme.[7-9] Such schemes require artificial dissipation to be added to control numerical oscillations. Upwind schemes can have several advantages over central difference schemes including natural numerical dissipation and better stability properties. The numerical scheme used here is an implicit scheme based on flux-splitting[10] and upwind spatial differencing in the streamwise direction.

Other factors that have direct impact on the 3-D numerical simulation are the geometric complexity and efficient management of large 3-D data sets. These factors make it necessary to develop zonal or patched methods where a large 3-D problem is divided into a number of smaller problems. Each smaller piece is then solved separately. The break-up of the large data base can be achieved in various ways.[11-14] Reference 11 and 12 are earlier applications

1

where the data base structure follows a pencil format. These numerical calcu-
lations, although promising, were based on limited computer resources. Refer-
ence 13 shows the development of a chimera grid scheme. This scheme provides
multiple regions where communications between grids are done by interpolating
in regions of overlap. A blocked grid approach reported by Belk, et al[14] does
not require interpolations at the interfaces. The schemes in References 13
and 14 are generally complicated since they allow for embedding a block or
zone into another. Recently, a simple composite grid scheme[15] has been
developed where a large single grid was partitioned into smaller grids. Each
of the smaller problems was solved separately with simple data transfers at
the interfaces. The initial results obtained were very promising. The
present effort extends the use of this composite grid scheme to include the
correct modeling of the base region of a projectile. Three-dimensional flow-
fields have been computed for two different projectiles over a transonic speed
range of $0.8 < M < 1.2$. Computed results show the critical aerodynamic
behavior.

II. NUMERICAL METHOD

1. GOVERNING EQUATIONS

The three-dimensional Navier-Stokes conservation equations of mass,
momentum, and energy can be represented in nondimensional flux vector form as:

$$\partial_\tau \hat{Q} + \partial_\xi(\hat{F} + \hat{F}_v) + \partial_\eta(\hat{G} + \hat{G}_v) + \partial_\zeta(\hat{H} + \hat{H}_v) = 0 \tag{1}$$

where the independent variable τ is the time and the spatial variables ξ, η, ζ
are chosen to map a curvilinear body conforming discretization into a uniform
computational space. Here $\hat{Q}$ contains all the dependent variables $[\rho, \rho u, \rho v,$
$\rho w, e]^T$ and $\hat{F}$, $\hat{G}$ and $\hat{H}$ are the inviscid fluxes. The flux terms $\hat{F}_v$, $\hat{G}_v$ and $\hat{H}_v$
contain the viscous derivatives. The conservative form of the equations is
used to capture the Rankine Hugoniot shock jump relations as accurately as
possible.

For body conforming coordinates and high Reynolds number flow where ζ is
the coordinate away from the surface, the thin layer approximation can be made
in the ζ direction. The governing equations can then be written as:

$$\partial_\tau \hat{Q} + \partial_\xi \hat{F} + \partial_\eta \hat{G} + \partial_\zeta \hat{H} = Re^{-1}\partial_\zeta \hat{S} . \tag{2}$$

Here the viscous terms in ζ have been collected into the vector $\hat{S}$ and the
nondimensional reciprocal Reynolds number is extracted to indicate a viscous
flux term. The viscous terms in ξ and η directions are neglected.

In differencing these equations it is often advantageous to difference
about a known base solution denoted by the subscript o as:

2

$$\delta_\tau(\hat{Q} - \hat{Q}_0) + \delta_\xi(\hat{F} - \hat{F}_0) + \delta_\eta(\hat{G} - \hat{G}_0) + \delta_\zeta(\hat{H} - \hat{H}_0)$$

$$- Re^{-1}\delta_\zeta(\hat{S} - \hat{S}_0) = -\partial_\tau\hat{Q}_0 - \partial_\xi\hat{F}_0 - \partial_\eta\hat{G}_0 - \partial_\zeta\hat{H}_0 + Re^{-1}\partial_\zeta\hat{S}_0 \tag{3}$$

where δ indicates a general difference operator, and ∂ is the differential operator. If the base state can be properly chosen, the differenced quantitatives can have smaller and smoother variation and therefore less differencing error. The freestream is used as a base solution in the present formulation.

2. IMPLICIT FINITE DIFFERENCE ALGORITHM

The implicit approximately factored scheme for the thin layer Navier-Stokes equations that uses central differencing in the η and ζ directions and upwinding in ξ is written in the form:

$$[I + h\delta_\xi^b(\hat{A}^+)^n + h\delta_\zeta\hat{C}^n - hRe^{-1}\overline{\delta}_\zeta J^{-1}\hat{M}^n J - D_i|_n]$$

$$\times [I + h\delta_\xi^f(\hat{A}^-)^n + h\delta_\eta\hat{B}^n - D_i|_n]\Delta\hat{Q}^n = -\Delta t\{\delta_\xi^b|(\hat{F}^+)^n - \hat{F}_\infty^+] + \delta_\xi^f|(\hat{F}^-)^n - \hat{F}_\infty^-] \tag{4}$$

$$+ \delta_\eta(\hat{G}^n - \hat{G}_\infty) + \delta_\zeta(\hat{H}^n - \hat{H}_\infty) - Re^{-1}\overline{\delta}_\zeta(\hat{S}^n - \hat{S}_\infty)\} - D_e(\hat{Q}^n - \hat{Q}_\infty)$$

where $h = \Delta t$ and the freestream base solution is used. Here δ is typically a three point second order accurate central difference operator, $\overline{\delta}$ is the midpoint operator used with the viscous terms, and the operators δ_ξ^b and δ_ξ^f are backward and forward three-point difference operators. The flux vector $\hat{F}$ has been split into $\hat{F}^+$ and $\hat{F}^-$, according to its positive and negative eigenvalues. The matrices $\hat{A}$, $\hat{B}$, $\hat{C}$ and $\hat{M}$ result from local linearization of the fluxes about the previous time level. Here J denotes the Jacobian of the coordinate transformation. Dissipation operators, D_e and D_i are used in the central space differencing directions.[6] The factored left hand side operators require inversion of tridiagonal matrices with 5 × 5 blocks. This two factor implicit scheme has been vectorized and can be readily multi-tasked in planes of ξ = constant.

3. COMPOSITE GRID SCHEME

In the present work, a composite grid scheme[15] has been used where a large single grid is split into a number of smaller grids so that computations can be performed on each of these grids separately. Each of these grids use the available core memory in turn, while the rest are stored on an external disk storage device such as the SSD of the Cray X-MP/48 computer. The Cray 2 supercomputer, has the large in core memory to fit the large single grid. However, for accurate geometric modeling of complex projectile configurations that include blunt noses, sharp base corners and base cavities, it is also

desirable to split the large data base into a few smaller zones on the Cray 2 as well.

A code developed for a single grid can be made to work for a block grid structure by: 1) mapping and storing the information for each grid onto a large memory; and 2) supplying interface boundary arrays, pointers and updating procedures. Consider the situation in Figure 1 in which the single grid from $J = 1$, J_{max} is partitioned into four grids (or zones), G1 through G4. The base region of the projectile is included by adding another zone G5. This procedure preserves the actual base corner. This zonal scheme has been modified to allow more than one zone in the wake for accurate modeling of other complicated base configurations including cavities.

The use of a composite or blocked grid scheme requires special care in storing and fetching the interface boundary data, i.e., the communication between the various zones. For the simple partitioning shown in Figure 1, all subgrid points are members of the original grid. There is no mismatch of the grid points at the interface boundaries and no interpolations are required. This procedure thus, has the advantage over-patched or overset grid schemes which do need interpolations. The partitioned grid has six interface boundaries, $J_1 = J_{1_{max}}$, $J_2 = 1$, $J_2 = J_{2_{max}}$, $J_3 = 1$, $J_3 = J_{3_{max}}$ and $J_4 = 1$ in the streamwise direction and two interface boundaries in the normal direction between grids G4 and G5. Data for these planes are to be supplied from the other grids by injecting interior values of the other grid onto the interface boundaries. The details of the data storage, transfer and other pertinent information such as metric and differencing accuracy can be found in Reference 15. Further details of differencing accuracy are presented next.

The differencing accuracy near the interfaces is quite important. Three point backward and forward difference operators are used at the interior points. Near the interface, for example, at $J_2 = J_{2_{max}} - 1$ a three point forward difference operator cannot be used with one grid point overlap as shown in Figure 1. The differencing accuracy can be dropped from second order to first order; however, this leads to inaccuracies in the flowfield solution near the interfaces.[15] To maintain second order accuracy near the interfaces, we difference, for example, $\dfrac{\partial F}{\partial \xi}$ at $J_2 = J_{2_{max}} - 1$ as,

$$\frac{\partial F}{\partial \xi} = \partial_\xi^b (F^+) + \partial_\xi^f (F^-)$$

where ∂_ξ^b is the usual three point backward difference operator and δ_ξ^f is now a central difference operator, i.e.,

$$\frac{\partial F}{\partial \xi} = \frac{3F_j^+ - 4F_{j-1}^+ + F_{j-2}^+}{2\Delta\xi} + \frac{F_{j+1}^- - F_{j-1}^-}{2\Delta\xi} \ .$$

4

Near the other interface of grid 2 ($J_2 = 2$), the ∂_ξ^b operator is correspondingly replaced by a central difference operator while ∂_ξ^f is a usual three point forward difference operator. The planes $J_2 = 1$ and $J_2 = J_{2_{max}}$ are, of course, boundaries for grid 2 and get their data from interior flowfield solutions from neighboring grids. Second order accuracy at and near the interfaces is thus, maintained. The use of central differencing near the interfaces has not adversely affected the stability of the scheme.

III. MODEL AND COMPUTATIONAL GRIDS

The first model used for the computational study presented here is an idealization of a realistic artillery projectile geometry. The experimental model shown in Figure 2 is a secant-ogive-cylinder-boattail (SOCBT) projectile. It consists of a three-caliber (cne-caliber = maximum body diameter), sharp, secant-ogive nose, a two-caliber cylindrical mid-section and a one-caliber 7° conical afterbody or boattail. A similar model was used for the computational studies with the only difference being a five percent rounding of the nose tip. The nose tip rounding was done for computational efficiency and is considered to have little impact on the final integrated forces. Experimental pressure data[16] are available for this shape and were obtained in the NASA Langley eight foot Pressure Tunnel using a sting mounted model. The test conditions of 1 atm supply pressure and 320 K supply temperature resulted in a Reynolds number of 4.5×10^6 based on model length.

The physical grid used for this computation is shown in Figure 3. Figure 3a shows the longitudinal cross section of the 3D grid while Figure 3b shows an expanded view of the three-dimensional base region grid. As shown in Figure 3a, the clustering of grid points near the body surface is done to resolve the viscous boundary layer near the body surface. Grid clustering has also been used in the longitudinal direction near the boattail and the base corners where large gradients in the flow variables are expected. In addition, the composite grid scheme preserves the sharp base corner. The grid consists of 202 points in the streamwise direction, 36 points in the circumferential direction and 50 points in the normal direction. This amounts to about 16 million words of storage for the code on the Cray X-MP/48. Only up to 4 Mw of central core memory was easily accessible; therefore, the full grid was partitioned into five smaller grids (including a base region grid) each of which would use the core memory in turn while the rest was stored on the SSD device. These computations were performed on the Cray X-MP/48 at the US Army Ballistic Research Laboratory (BRL). Each numerical simulation (includes all partitioned grids) took over 20 hours of computer time.

A second grid, shown in Figure 4, was obtained to simulate the actual experimental SOCBT configuration which includes a sting in the base region. This view is again a longitudinal cross-section of the 3-D grid. The grid is wrapped around the base corner in this case. It consists of 238 points in the axial direction, 39 points in the circumferential direction and 50 points in the normal direction. Computations on this grid were performed on the Cray 2 computer at BRL using the same code. The computing time for each of these simulations was 20-30 hours.

5

The second projectile under consideration is the M549 projectile shown in Figure 5. This projectile has a short boattail of about 1/2 a caliber in length. For simplicity, the flat nose was again modeled with nose tip rounding and the rotating band was eliminated. Aerodynamic coefficient data[17-19] are available for this configuration and were used for comparison. Computations for this projectile have been made for atmospheric flight conditions. Figure 6 shows an expanded view of the grid around this projectile and shows both the wind-side and lee-side planes. The full grid consists of 298 points in the axial direction, 39 points in the circumferential direction and 50 points in the normal direction. Calculations for this projectile were performed on the Cray 2 computer at BRL. Each of these calculations took over 30 hours of computer time.

IV. RESULTS

The implicit time marching procedure was used to obtain the desired steady state result. Initial conditions were freestream everywhere and the boundary conditions were updated explicitly at each time step. The solution residual dropped at least three orders of magnitude before converged solutions were obtained. In addition, the surface pressure distributions were checked for time invariance. For the computation of turbulent flow, a turbulence model must be supplied. In the present calculation, a two layer algebraic eddy viscosity model due to Baldwin and Lomax[20] was used. Results are now presented for two cases: (1) SOCBT projectile with and without sting; and (2) M549 projectile.

1. SOCBT PROJECTILE, $0.9 < M_\infty < 1.2$, $\alpha = 4$

Results have been obtained at various transonic speeds for both cases with and without modeling of the sting. Figures 7-10 show the Mach contours for the projectile in the wind-ward and lee-ward planes. These figures show the expansions at the ogive-cylinder and cylinder-boattail corners. These figures indicate the presence of shock waves on the cylinder and also on the boattail which typically occur on the projectile at transonic speeds. Sharp shocks are observed on the boattail. These boattail shocks are shown to be longitudinally asymmetric due to the influence of angle of attack. The asymmetry can also be seen in the wake flow behind the bluff base. As the Mach number is increased from 0.94 to 0.96 and then to 0.98, the shocks become stronger and move towards the base of the projectile. At higher transonic speeds past the speed of sound (see Figure 10), these shocks become weak; however, a bow shock forms in front of the nose of the projectile.

Computations have also been made to investigate the effect of the sting on the transonic projectile flowfield. A typical plot of Mach contours for this simulation is shown in Figure 11a for $M_\infty = 0.96$ and $\alpha = 4°$. As expected, the sting has a large effect on the qualitative features of the flow field in the wake region. An experimentally obtained shadowgraph at the same flow conditions is shown in Figure 11b. The actual shock wave position is the front of the structure shown in this shadowgraph. As shown in Figures 11a and 11b, the agreement between the computation and experiment for the shock wave positions is good. Figures 12a and 12b show the wind-side and lee-side velocity vectors in the base region for both configurations. Figure 12a is for the case with no sting whereas Figure 12b includes the sting in the base region. In both

6

cases, asymmetry in the flowfield can be observed between the wind-side and lee-side. Three pairs of separated flow bubbles can be seen in the near wake for the case of no sting (Figure 12a). For the case with sting (Figure 12b), one can see the large primary bubble along with a counter rotating small bubble near the junction of the sting and the base. The primary bubble is more elongated on the wind-side and the flow reattaches further downstream of the base.

Figures 13-15 show the surface pressure distributions as a function of the longitudinal position and are compared with experimental data.[16] Figures 13a and 13b show the comparison at $M_\infty = 0.96$ for the wind-side and lee-side, respectively. Computed results are shown for two grids, one which wrapped around the base corner and the other which did not. As shown in these figures, the computed results are virtually the same for both computations except near the base corner where a small difference can be noticed. The agreement of computed surface pressure with experimental data is good for the wind-side. On the lee-side, the agreement is good only on the ogive nose and small discrepancy can be seen on the cylinder as well as on the boattail. The expansions and recompressions near the ogive-cylinder and cylinder-boattail junctions have been captured. Figures 14a and 14b show the surface pressure distribution for $M_\infty = 0.98$. Computed results are shown for both cases with and without sting for turbulent flow. In the experiment,[16] the model was sting mounted and no boundary layer trip was used. Therefore, it is not clear if the flow was laminar or turbulent. Computed results were obtained for the sting mounted case for both laminar and turbulent flow conditions and compared with experimental data. Comparison of the pressure on the wind-side (Figure 14a) shows generally good agreement of the computed pressure with the experimental data. The largest differences between the computed results are seen on the rear part of the boattail where no experimental results are available. The comparison on the lee-side (Figure 14b) again shows good agreement of the computed result with experimental data for most of the projectile except on the second half of the boattail. As expected, the computed result with no sting has the largest discrepancy. Computed results with sting simulation compare well with experimental data especially for laminar flow conditions. The difference in computed pressures on the nose and the cylinder between the sting case and no sting case is a result of different grids used. A typical result at a high transonic speed $M_\infty = 1.1$ is shown in Figure 15. The agreement of the computed surface pressures with experiment is very good. At this high transonic Mach number, the shocks on the cylinder as well as on the boattail are very weak as evidenced by the absence of a sharp rise in pressure in those areas. The expansions and recompressions near the ogive-cylinder and cylinder-boattail junctions can be clearly observed in Figure 15.

The computed surface pressures have been integrated to obtain the aerodynamic forces and moments. The slope of the pitching moment coefficient (C_{m_α}) is generally of greater concern in projectile aerodynamics since it is the parameter that determines the static stability of the projectile. Figure 16 shows the variation of the slope of the pitching moment coefficient with Mach number. It clearly shows the critical aerodynamic behavior in the transonic speed regime, i.e., the sharp rise in the coefficient between $M = 0.92$ and 0.96 and its subsequent sharp drop. This is followed by a smooth decrease in the coefficient as Mach number is increased further. The increase in C_{m_α}

7

between M = 0.92 and 0.96 is of the order of 20% which is a typical value obtained from a number of range tests for similar projectiles.

2. M549 PROJECTILE, 0.7 < M_∞ < 1.5, α = 2

Numerical computations were made for the M549 projectile at various transonic speeds, 0.7 < M_∞ < 1.5 and at angle of attack, α = 2°. Qualitative features of the flowfield obtained from some of these calculations are shown in Figures 17-21 where Mach number contours have been plotted for M = 0.85, 0.90, 0.92, 0.94, and 0.98 for both wind-ward and lee-ward planes. The asymmetry in the wake region flow is obvious from these figures. These figures indicate the development and asymmetric locations of shock waves on the projectile at transonic speeds. At low transonic speeds, for example, at M = 0.85 (Figure 17) the shock waves are just beginning to form especially near the boattail junction. As Mach number is increased to M = 0.90, the shocks are already formed on the projectile both near the cylinder as well as boattail junctions. The flow expansions at these junctions can also be clearly seen in this figure. The small asymmetry in shockwave locations can be observed particularly with the boattail shocks. The wind-side shockwave on the boattail is a little closer to the base than its counterpart on the lee-side. In addition, these shocks have moved downstream from the boattail junction. As shown in Figures 19-21, with further increase in Mach number to 0.92, 0.94, and 0.98, the shock waves (both on the cylinder and the boattail) become stronger and gradually move downstream. The asymmetry in the location of the shock waves become more apparent as the Mach number is increased. It is this asymmetry which gives rise to the critical aerodynamic behavior. As seen in Figure 21 for M = 0.98, the shock wave pattern is complicated and the boattail shocks are located very close to the base corners.

The static aerodynamic coefficients have been obtained from the computed flowfields. As pointed out earlier, the slope of moment coefficient (C_{m_α}) is of primary concern. Figure 22 shows the development of C_m over the projectile for various transonic speeds. Actually, it is the accumulative moment coefficient referenced to the nose and thus, the value at the end (X/D = 5.645) is the final result. The difference in this coefficient over the nose portion is practically negligible for all transonic Mach numbers. The largest effect is seen on the cylinder and boattail sections. The boattail has a dramatic effect as evidenced by the sharp rise in all the curves. Figure 23 shows the C_{m_α} comparison between the computation and the available data.[17-19] Here C_{m_α} is referenced to center of gravity (C.G.) of the projectile. One can clearly see the sharp rise in C_{m_α} between M = 0.7 to 0.94 which is followed by the sharp drop with further increase in Mach number in both the computation and the data. This critical aerodynamic behavior observed in the data is clearly predicted in the computations. Earlier data by Kline, et al[17] is shown in circles and is a compliation of wind tunnel and free flight range data. More recent data for this projectile has been obtained from BRL range firings by Whyte, et al[18] and is shown in squares. Each of these data points comes from a six degree of freedom (DOF) single fit procedure. The computed results agree well with the data by Kline, et al[18] for M > 1.1. The computed results overpredict Whyte's data by 5-7% at high transonic speeds, 1.0 < M < 1.4.

8

Some discrepancy can also be observed at low transonic speeds M < 0.9. However, the discrepancy is again of the order of 5-7%. Flight data for transonic region is no better than 7%[19] due to rapid variation of C_{m_α} with Mach number. Thus, the computed results are well within the experimental accuracy at these transonic speeds.

V. CONCLUDING REMARKS

In conjunction with a new Navier-Stokes code, a simple composite grid scheme has been developed. This capability allows the use of fine computational grids needed for accurate transonic flow computations on CRAY X-MP/48 or Cray 2 computers. The numerical method uses an implicit, approximately factored, partially upwind (flux-split) algorithm.

The three dimensional transonic flowfield computations have been made for two projectiles for different flow conditions and angle of attack. The computed flowfields show the development of the asymmetrically located shock waves on the projectile at various transonic speeds. For the SOCBT projectile, computed surface pressures have been compared with experimental data and are found to be in good agreement. The slope of the pitching moment coefficient (C_{m_α}), determined from the computed flowfields, shows the critical aerodynamic behavior. The computed C_{m_α} for the M549 projectile has been compared with available data. Again, the computed results show the same critical behavior seen in the data. The discrepancy between the computed result and data is less than seven percent.

The results of this research provide the basis for a new capability to compute three dimensional transonic flowfields over projectiles. This capability in conjunction with the supercomputers at BRL has led to the first successful prediction of the critical aerodynamic behavior in C_{m_α} of artillery shell at transonic speeds. The next step is the numerical prediction of Magnus force and moment for spinning projectiles at angle of attack. This involves calculations of the full three dimensional flowfield with no plane of symmetry.
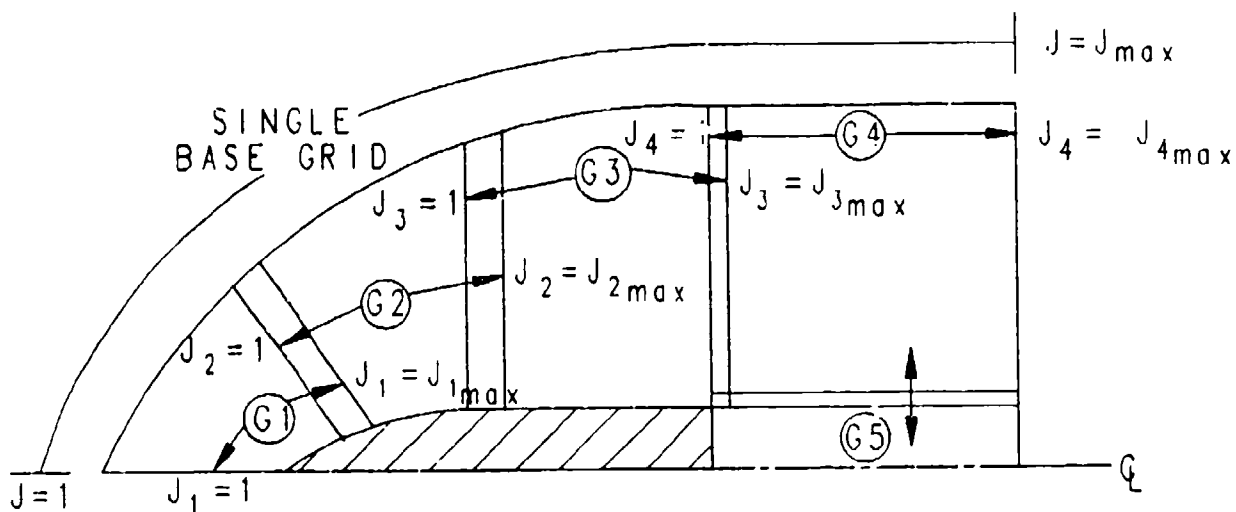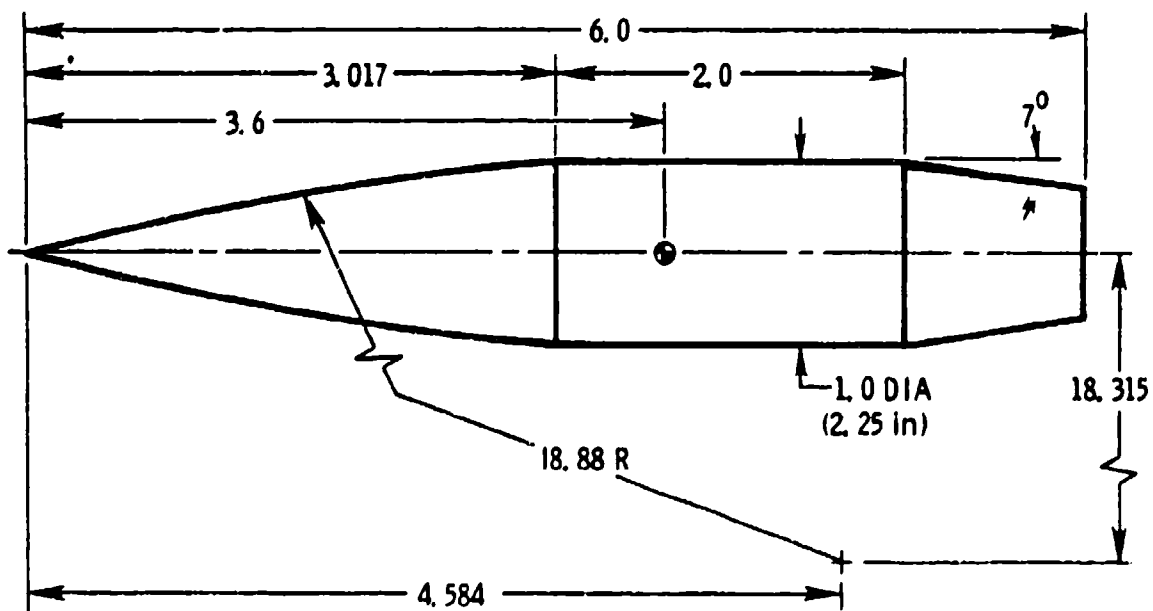
9

Figure 1. Schematics of grid partitioning.

ALL DIMENSIONS IN CALIBERS

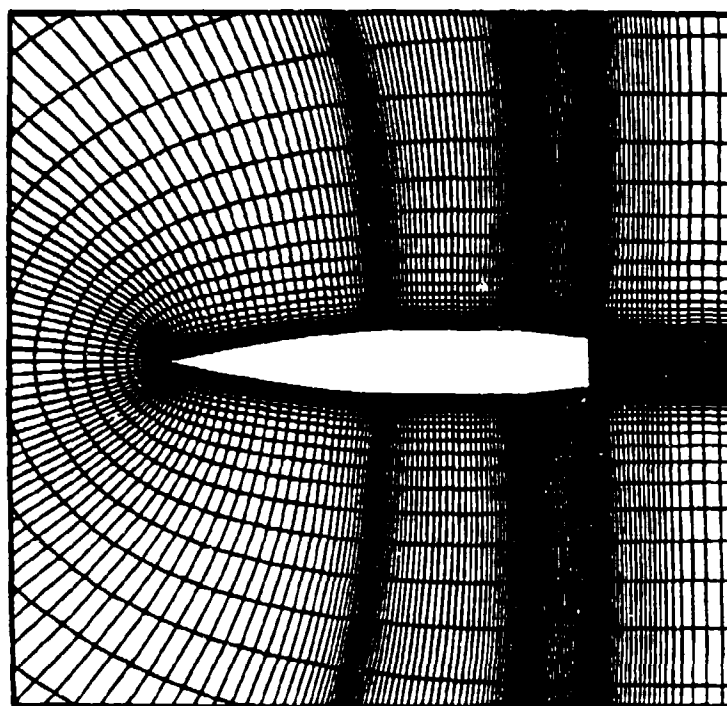Figure 2. Model geometry of the SOCBT projectile.

10

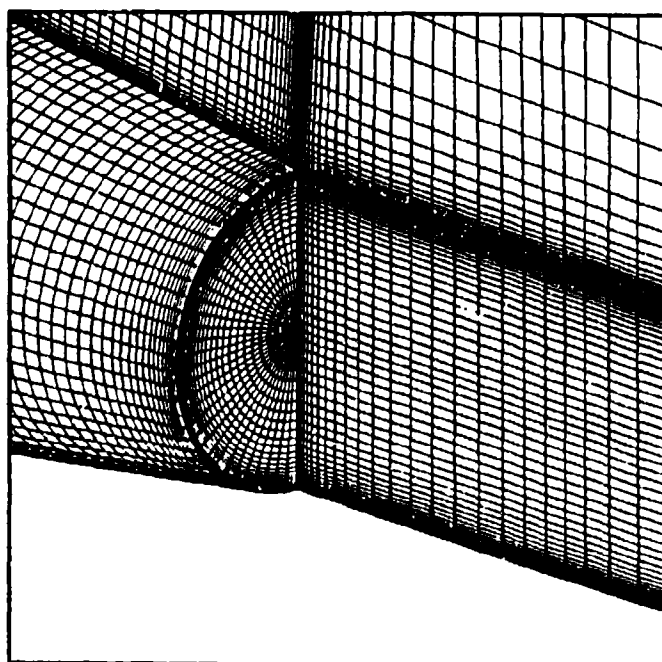Figure 3a. Longitudinal cross-section of the 3D grid.

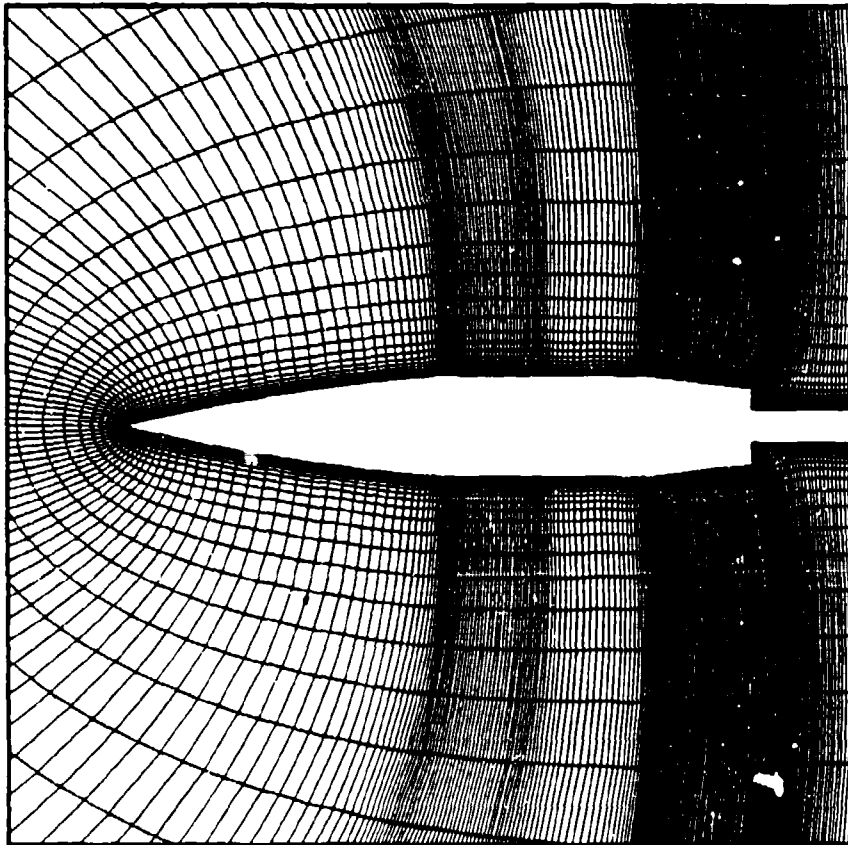Figure 3b. Expanded view of the base region grid.

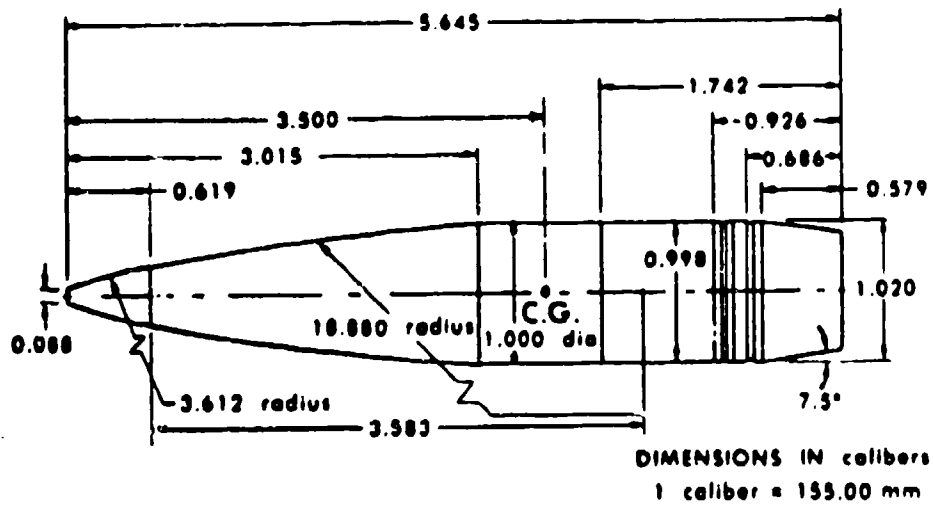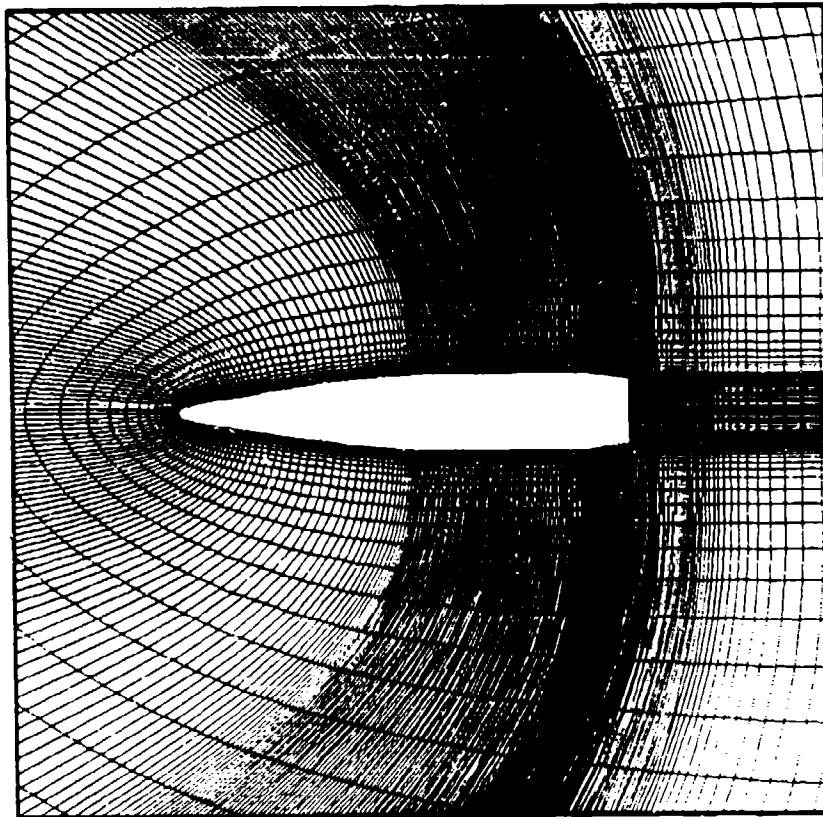Figure 4. Grid for the sting mounted SOCBT projectile.

Figure 5. M549 projectile.

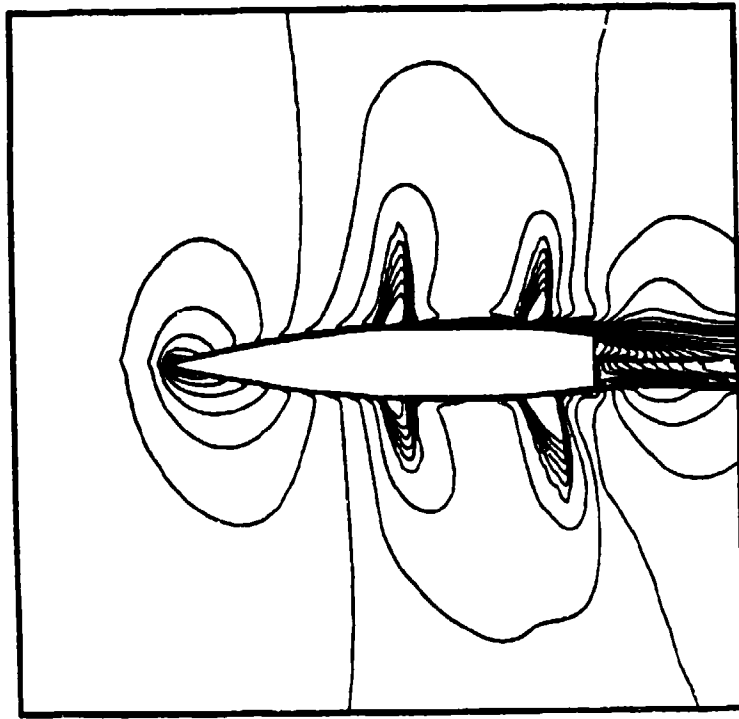Figure 6. Longitudinal cross-section of the grid for M549 projectile.

13

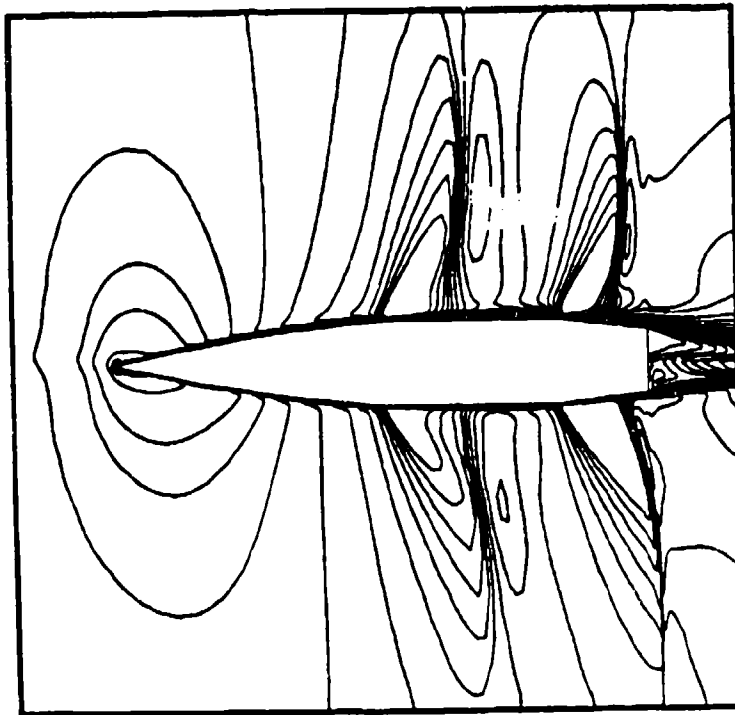Figure 7. Mach contours, SOCBT projectile, $M_\infty = 0.94$, $\alpha = 4°$.

Figure 8. Mach contours, SOCBT projectile, $M_\infty = 0.96$, $\alpha = 4°$.

14
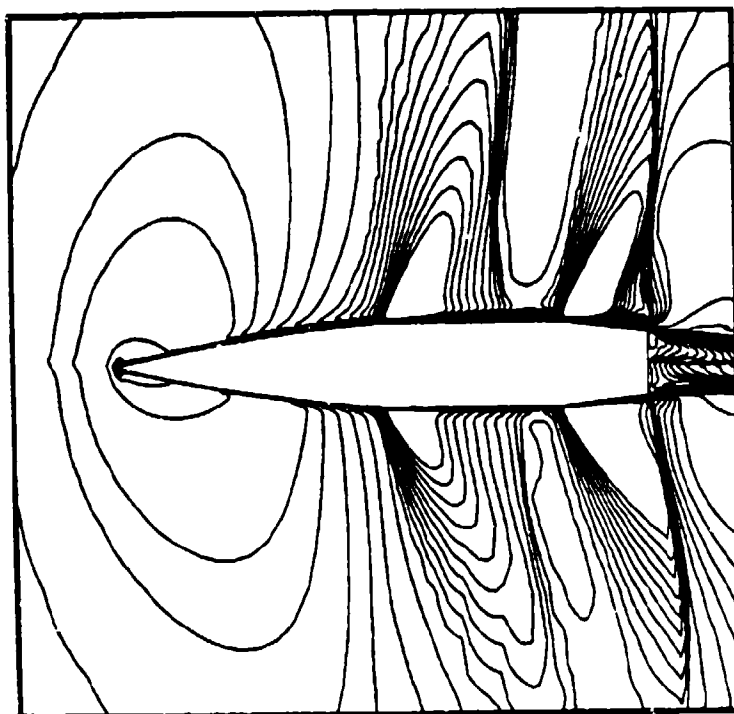
Figure 9. Mach contours, SOCBT projectile, $M_\infty = 0.98$, $\alpha = 4°$.

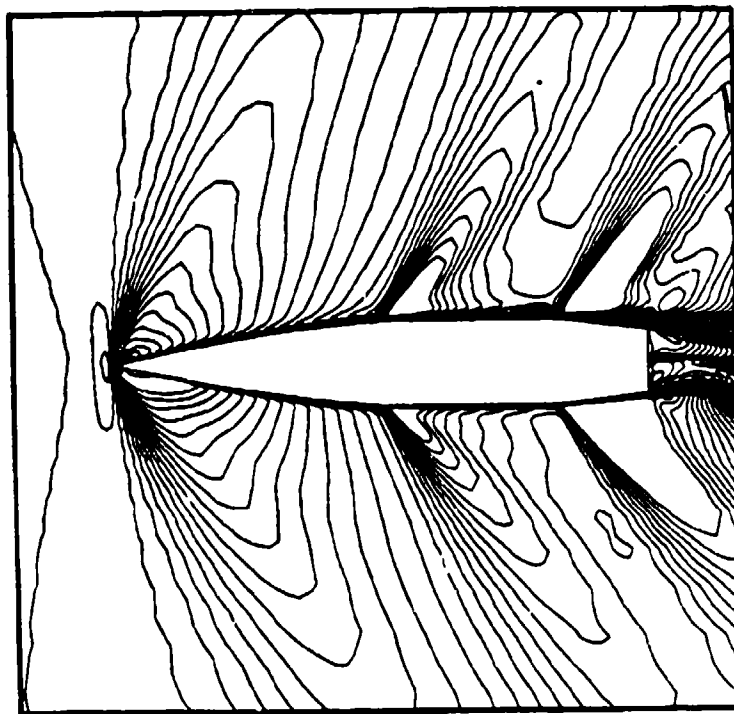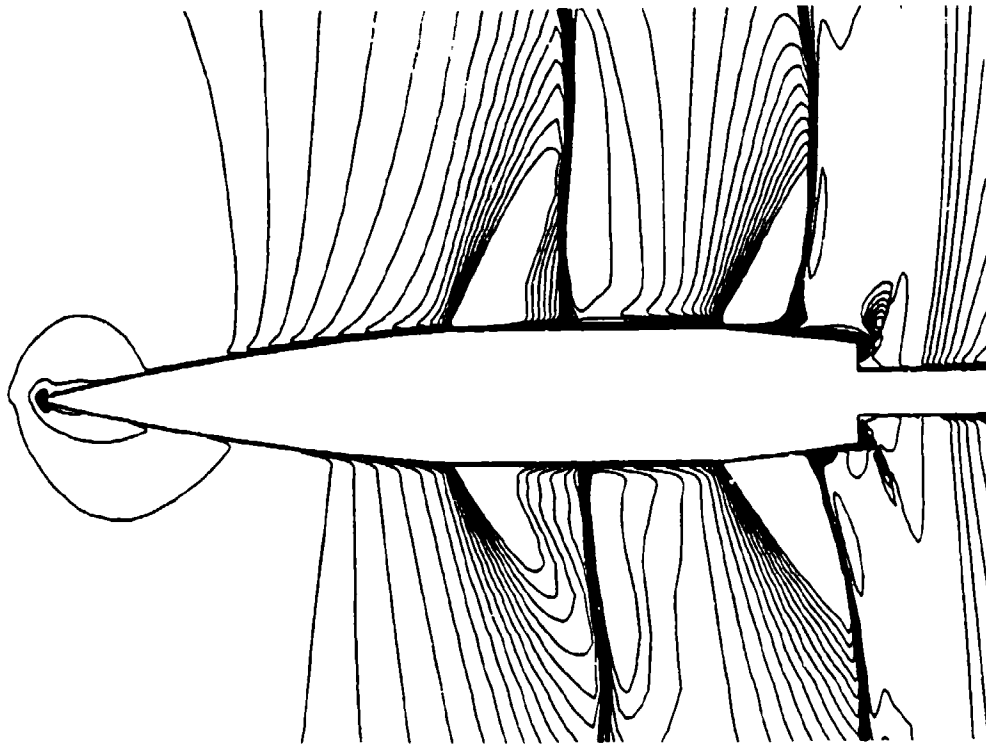Figure 10. Mach contours, SOCBT projectile, $M_\infty = 1.1$, $\alpha = 4°$.

15

Figure 11a. Computed Mach contours, $M_\infty = 0.96$, $\alpha = 4°$,
SOCBT projectile (with sting).
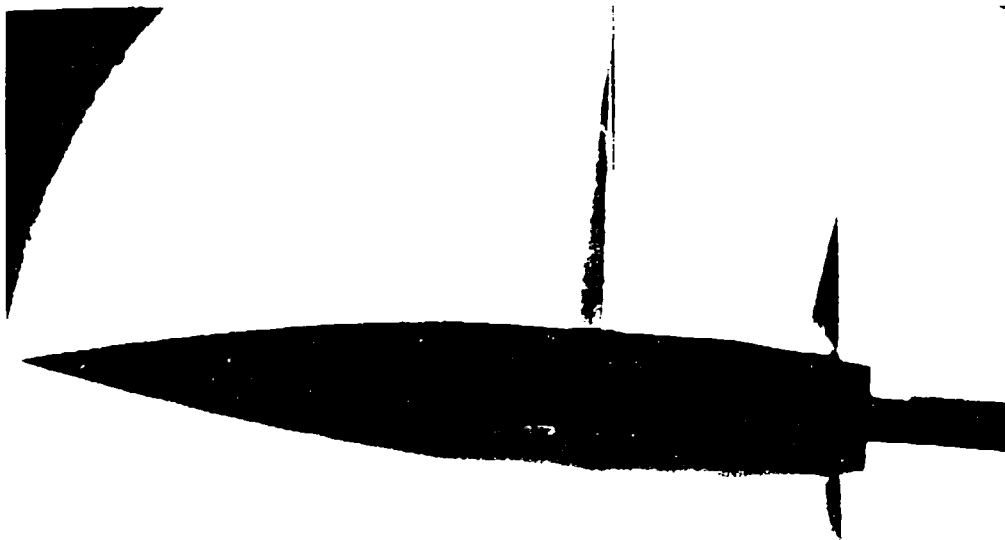

Figure 11b. Experimental shadowgraph, $M_\infty = 0.96$, $\alpha = 4°$,
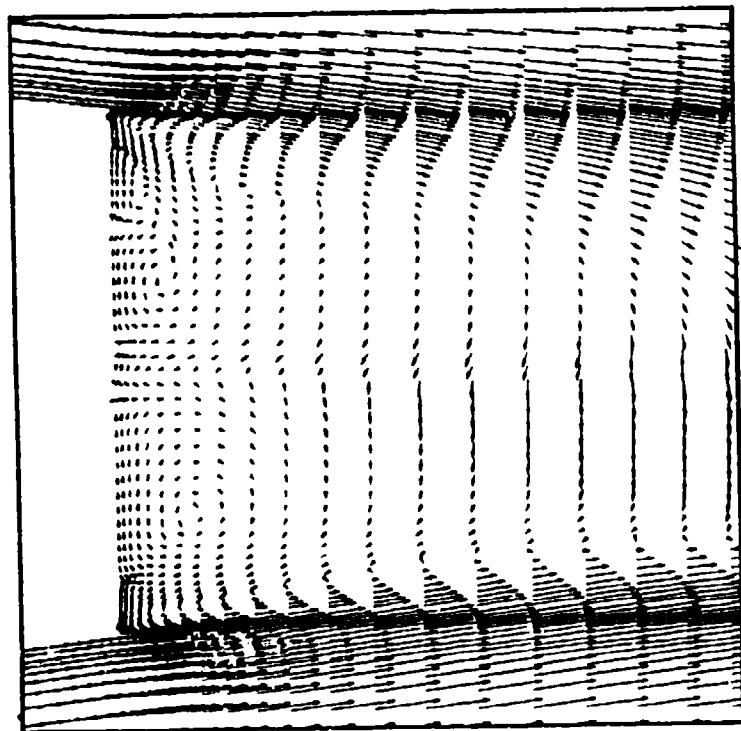SOCBT projectile (with sting).

Figure 12a. Velocity vectors in the base region, $M_\infty = 0.96$, $\alpha = 4°$, SOCBT projectile (without sting).
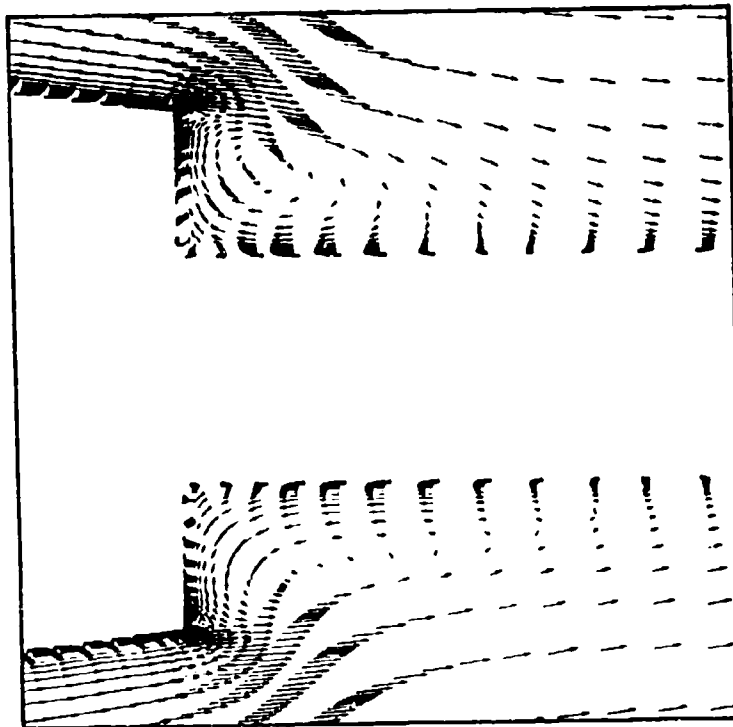

Figure 12b. Velocity vectors in the base region, $M_\infty = 0.96$, $\alpha = 4°$, SOCBT projectile (with sting).

Figure 13a. Longitudinal surface pressure distribution, SOCBT projectile, $M_\infty = 0.96$, $\alpha = 4°$, wind-side.

Figure 13b. Longitudinal surface pressure distribution, SOCBT projectile, $M_\infty = 0.96$, $\alpha = 4°$, lee-side.
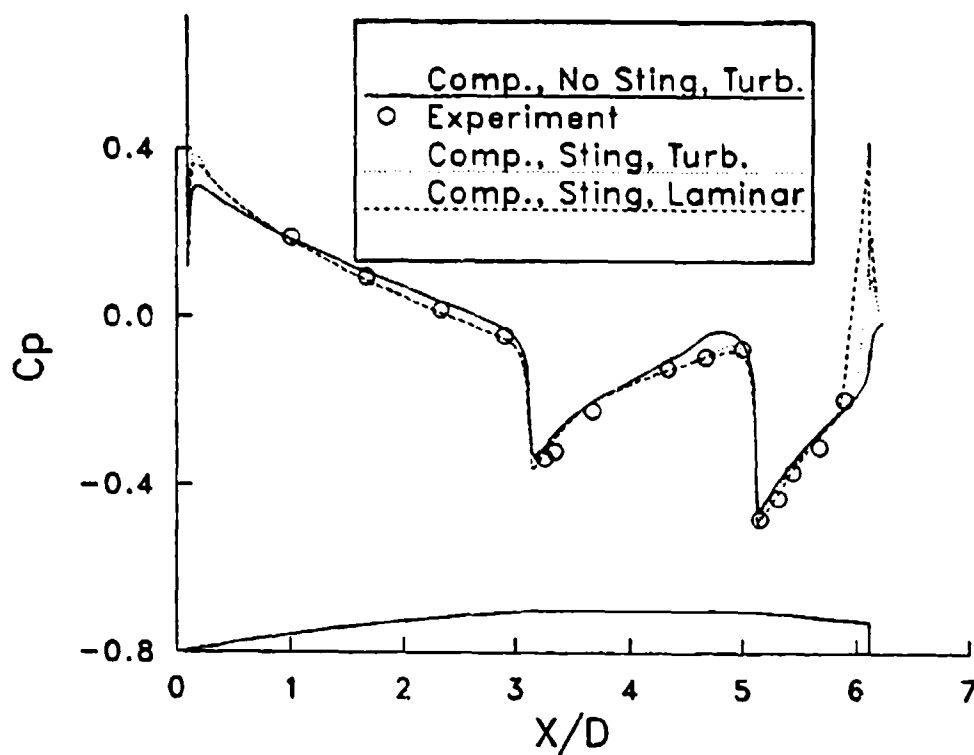
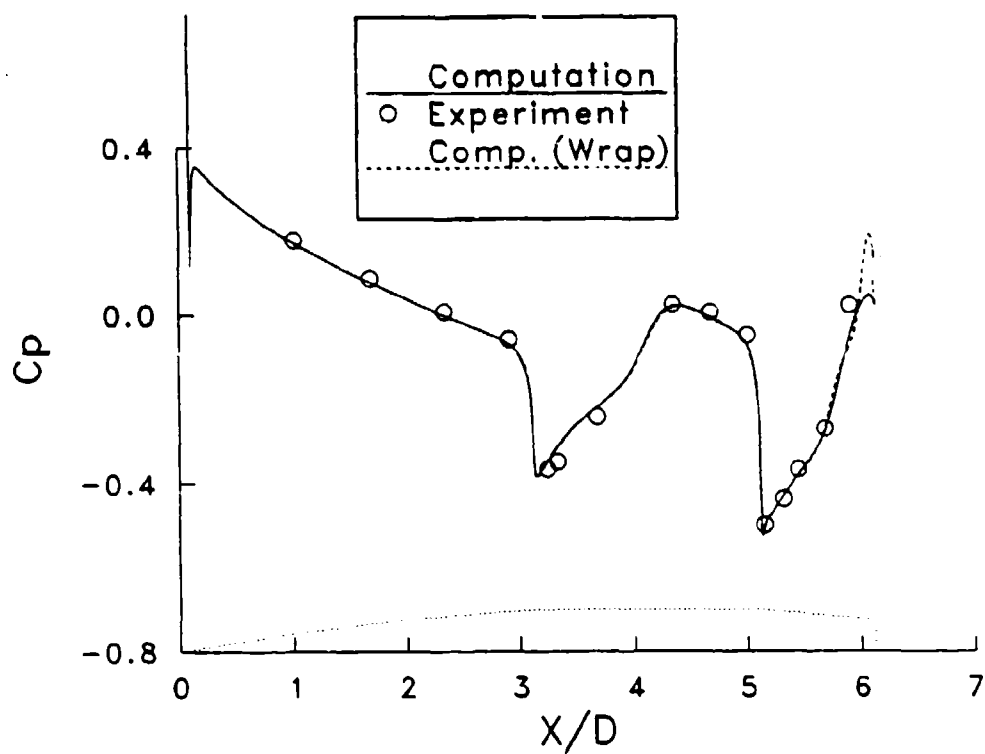Figure 14a.   Longitudinal surface pressure distribution, SOCBT projectile,
$M_\infty = 0.98$, $\alpha = 4°$, wind-side.
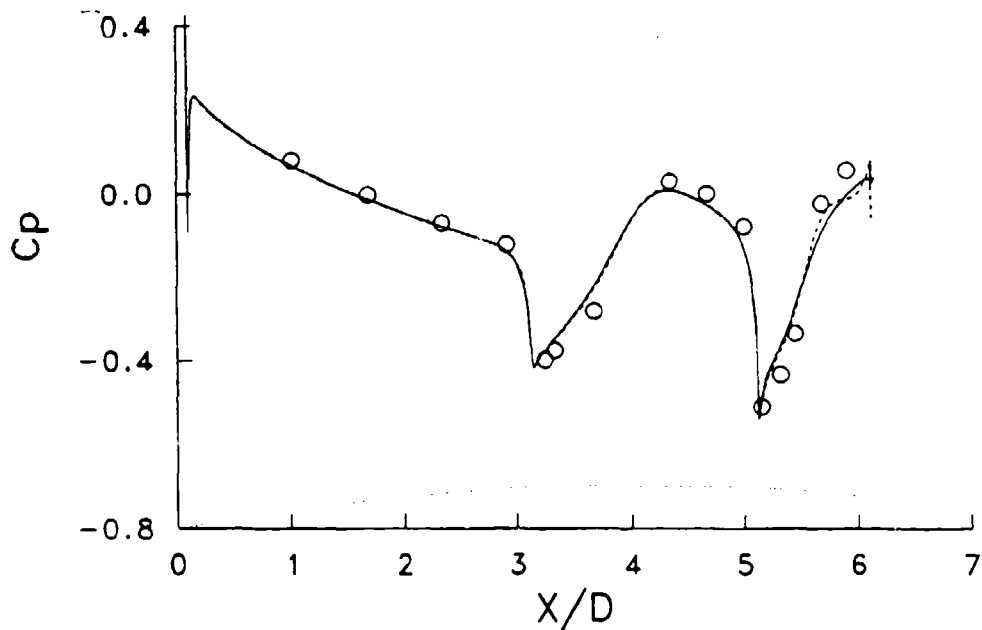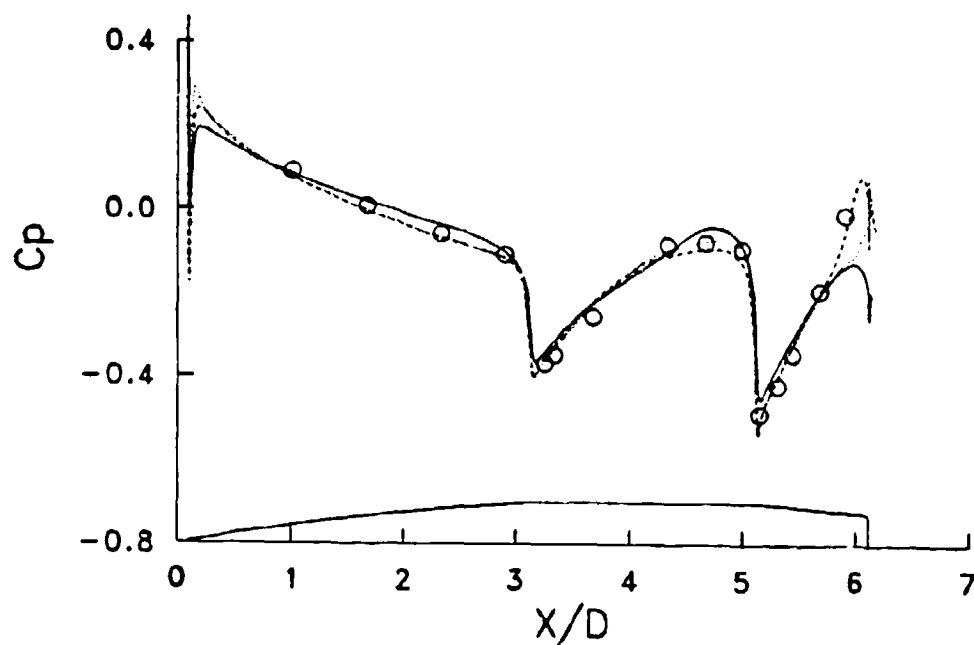

Figure 14b.   Longitudinal surface pressure distribution, SOCBT projectile,
$M_\infty = 0.98$, $\alpha = 4°$, lee-side.

19
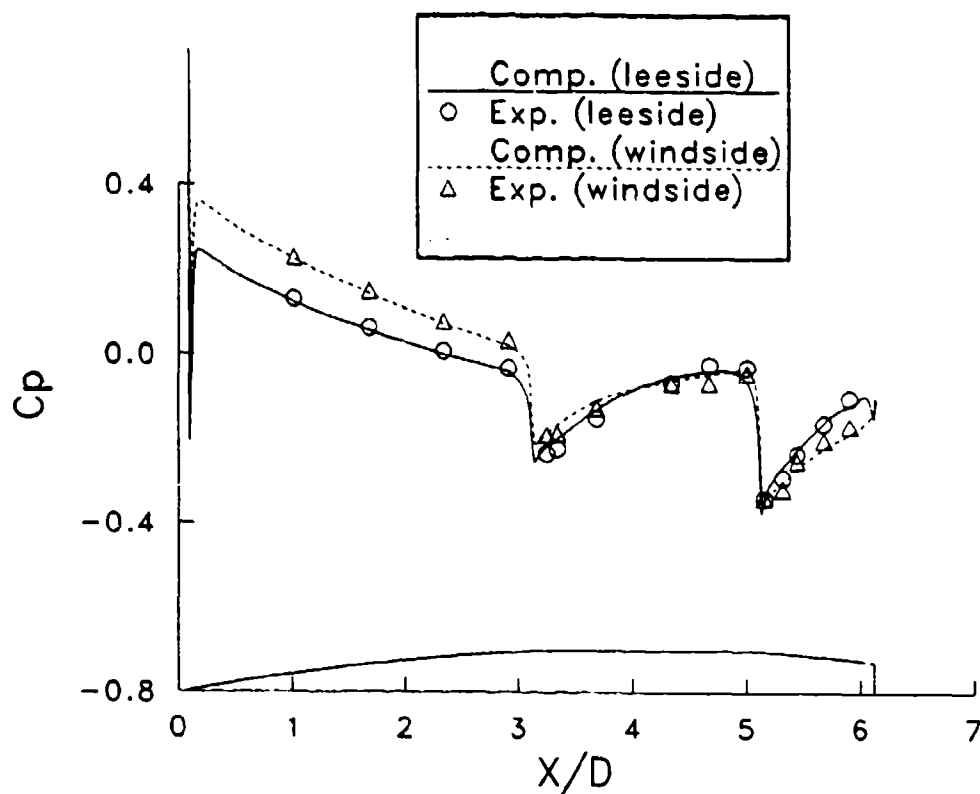
Figure 15. Longitudinal surface pressure distribution, SOCBT projectile, $M_\infty - 1.1$, $\alpha = 4°$.
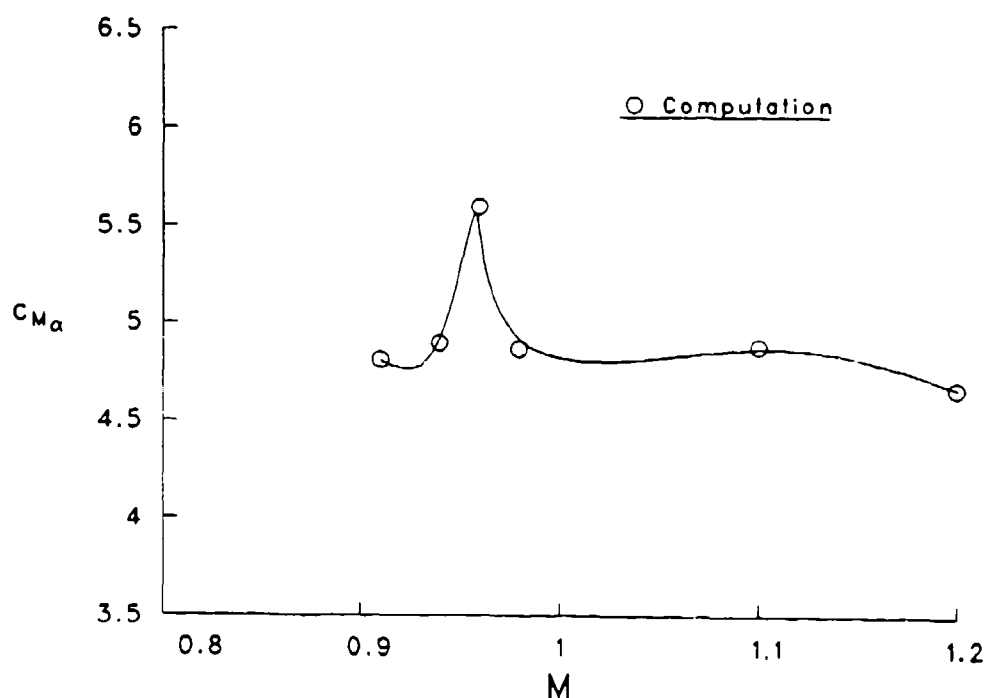
Figure 16. Slope of pitching moment coefficient, C_{m_α}, vs Mach number, SOCBT projectile.
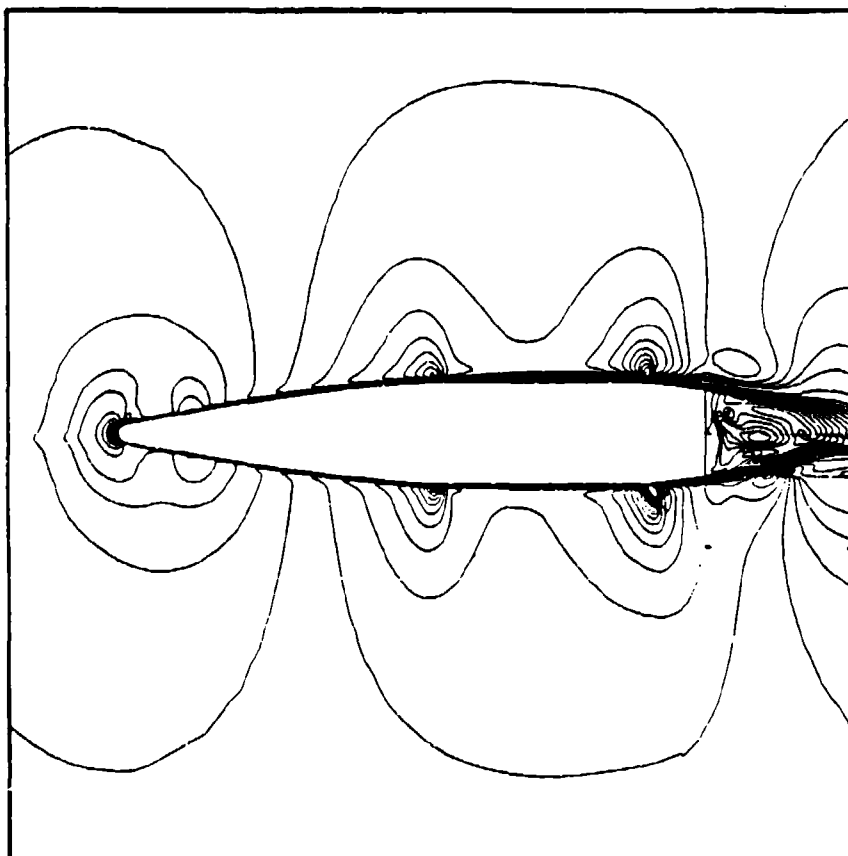
Figure 17.   Mach contours, M549 projectile, $M_\infty = 0.85$, $\alpha = 2°$.
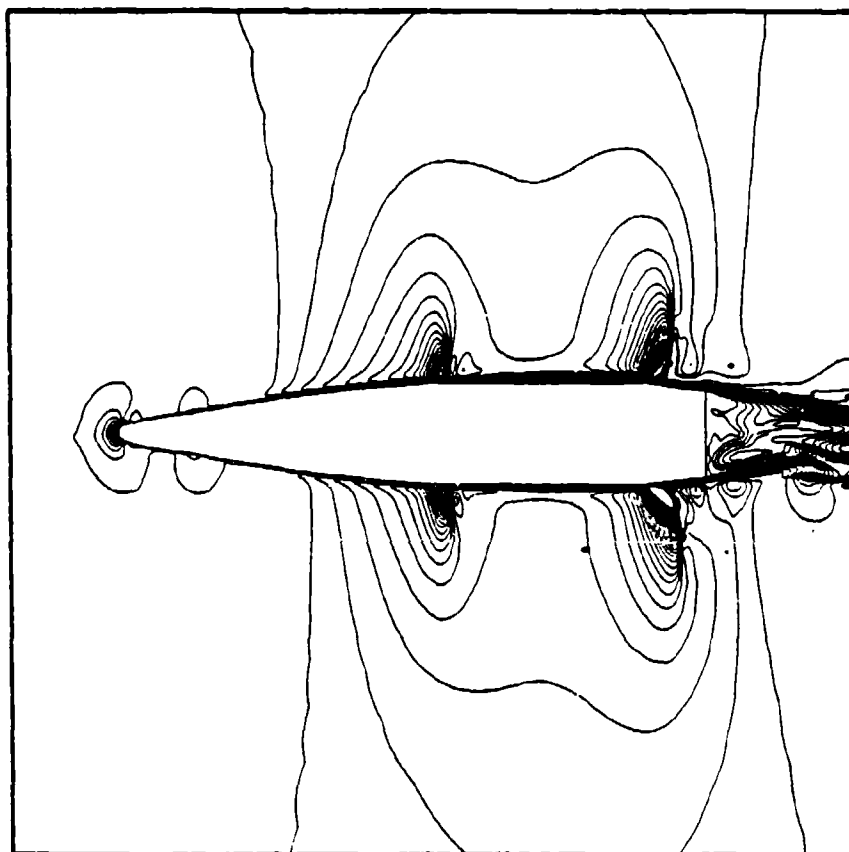
Figure 18. Mach contours, M549 projectile, $M_\infty = 0.90$, $\alpha = 2°$.
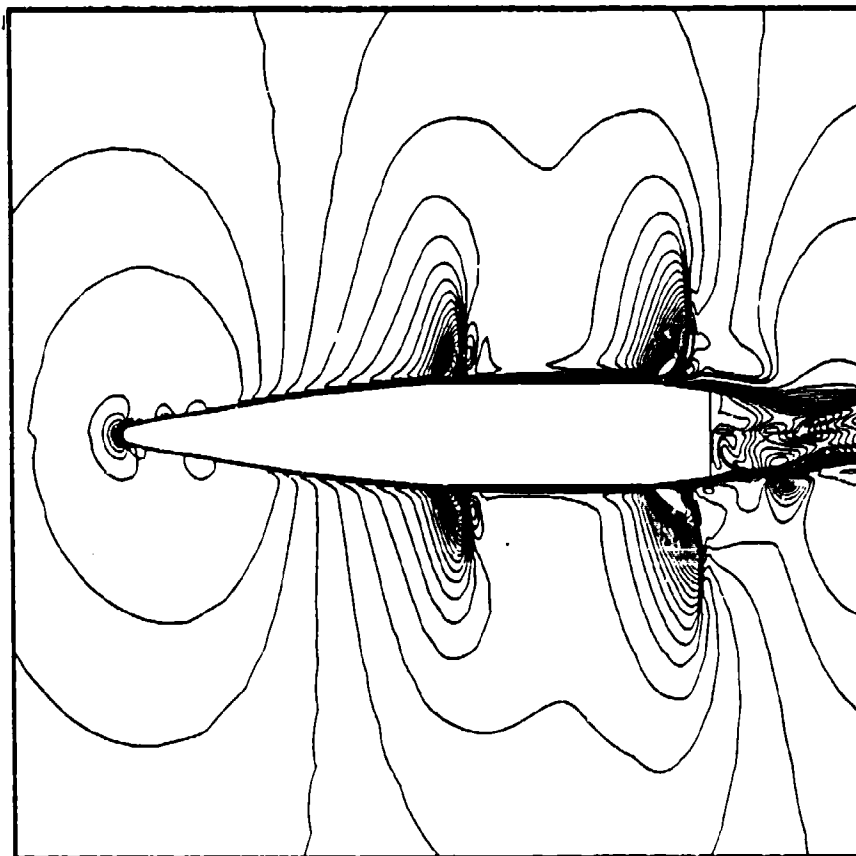
Figure 19.   Mach contours, M549 projectile, $M_\infty = 0.92$, $\alpha = 2°$.
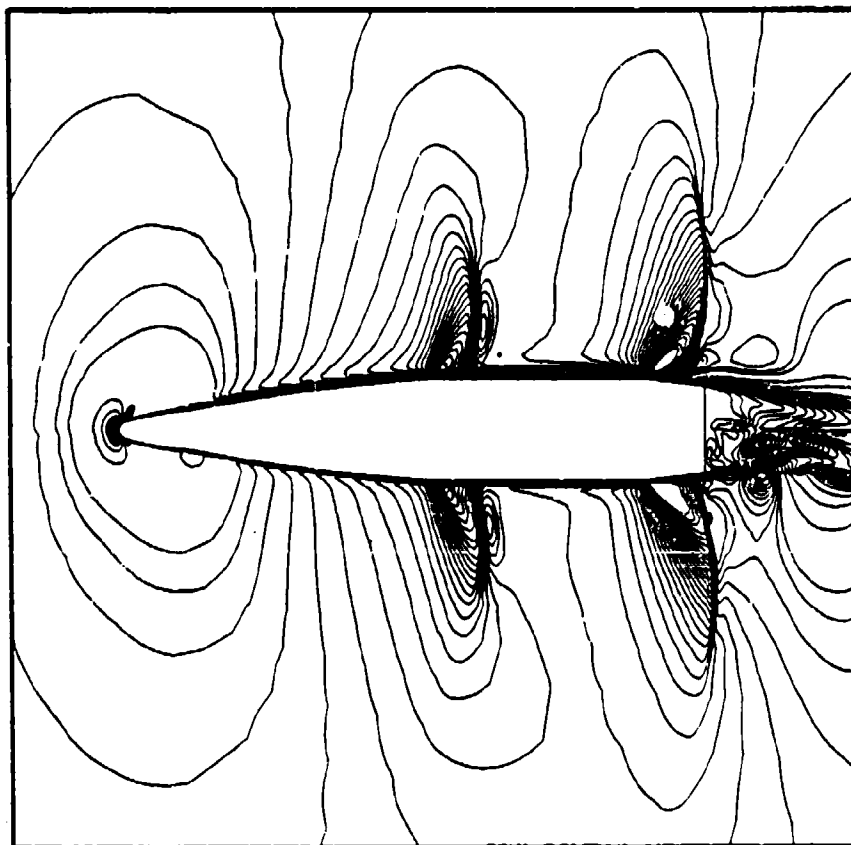
Figure 20.   Mach contours, M549 projectile, $M_\infty = 0.94$, $\alpha = 2°$.
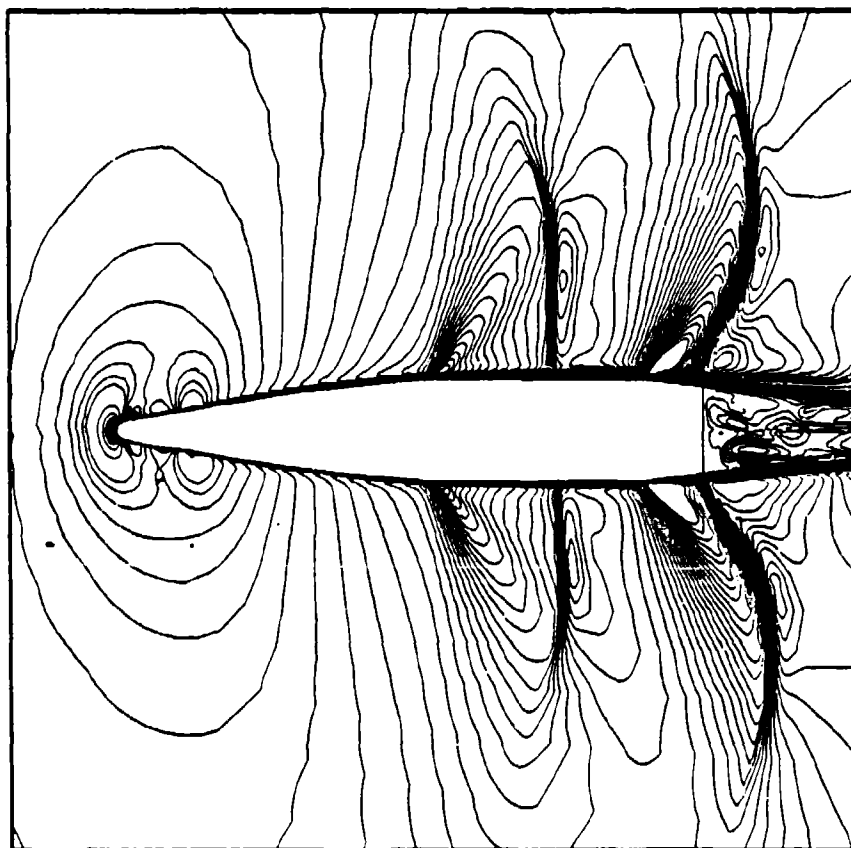
Figure 21.   Mach contours, M549 projectile, $M_\infty = 0.98$, $\alpha = 2°$.

Figure 22. Development of pitching moment coefficient over the M549 projectile, $\alpha = 2°$.

Figure 23. Slope of pitching moment coefficient, C_{m_α} vs Mach number, M549 projectile.

26

REFERENCES

1. Deiwert, G.S., "Numerical Simulation of Three Dimensional Boattail After-body Flowfield," AIAA Journal, Vol. 19, May 1981.

2. Nietubicz, C.J., Sturek, W.B., and Heavey, K.R., "Computations of Projectiles Magnus Effect at Transonic Velocities, AIAA Journal, Vol. 23, No. 7, July 1985.

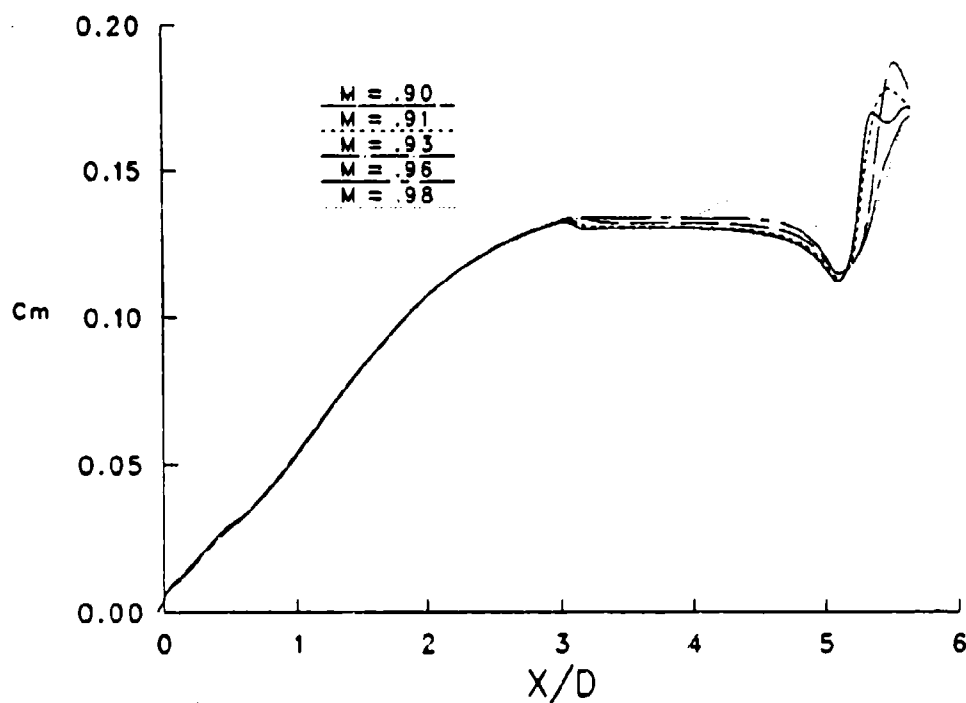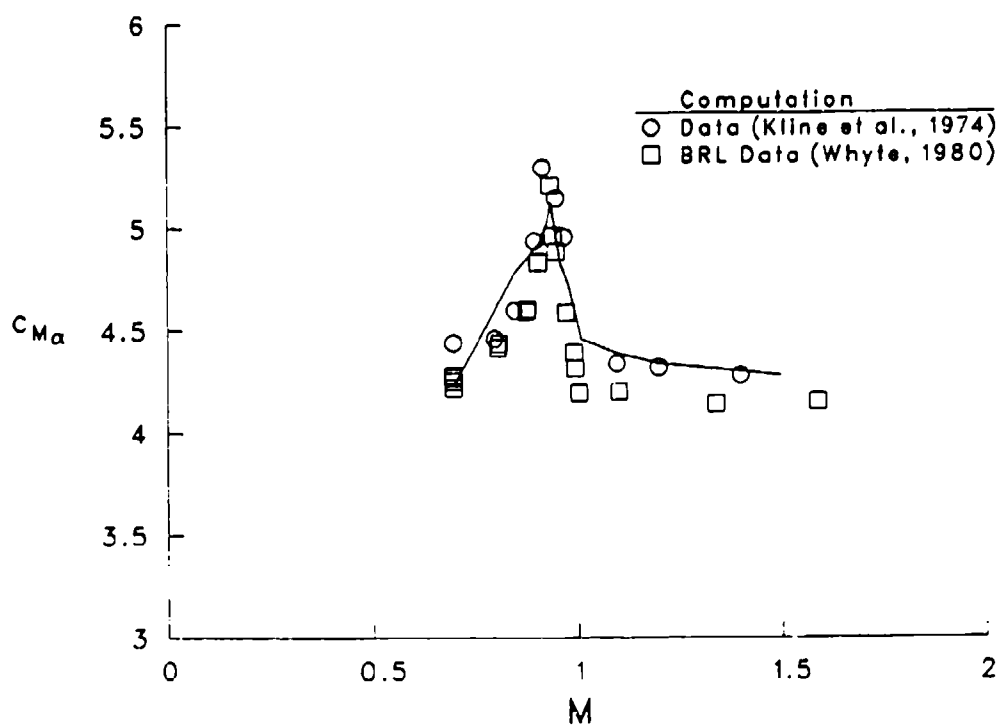3. Nietubicz, C.J., Sahu, J. and Lafarge, R., "Aerodynamic Coefficient Predictions for a Projectile Configuration at Transonic Speeds," BRL-MR-3639, US Army Ballistic Research Laboratory, Aberdeen Proving Ground, Maryland, December 1987.

4. Sahu, J., Nietubicz, C.J. and Steger, J.L., "Navier-Stokes Computations of Projectile Base Flow With and Without Base Injection," ARBRL-TR-02532, US Army Ballistic Research Laboratory, Aberdeen Proving Ground, Maryland, November 1983. (AD A135738) (See also AIAA Journal, Vol. 23, No. 9, September 1985, pp. 1348-1355.)

5. Sahu, J., "Three Dimensional Base Flow Calculation for a Projectile at Transonic Velocity," AIAA Paper No. 86-1051, May 1986.

6. Ying, S.X., Steger, J.L., Schiff, L.B. and Baganoff, D., "Numerical Simulation of Unsteady, Viscous, High-Angle-of-Attack Flows Using a Partially Flux-Split Algorithm," AIAA Paper No. 86-2179, August 1986.

7. Beam, R. and Warming, R.F., "An Implicit Factored Scheme for the Compressible Navier-Stokes Equations," AIAA Paper No. 85-1815-CP, August 1985.

8. Steger, J.L., "Implicit Finite Difference Simulation of Flow About Arbitrary Geometries with Application to Airfoils," AIAA Journal, Vol. 16, No. 4, July 1978, pp. 679-686.

9. Pulliam, T.H. and Steger, J.L., "On Implicit Finite-Difference Simulations of Three-Dimensional Flow, AIAA Journal, Vol. 18, No. 2, February 1980, pp. 159-167.

10. Steger, J.L. and Warming, R.F., "Flux Vector Splitting of the Inviscid Gasdynamic Equations with Application to Finite-Difference Methods," Journal of Computational Physics, Vol. 40, No. 2, 1981, pp. 263-293.

11. Lomax, H. and Pulliam, T.H., "A Fully Implicit Factored Code for Computing Three Dimensional Flows on the ILLIAC IV, Parallel Computations," G. Rodrigue Ed., Academic Press, New York, 1982, pp. 217-250.

12. Deiwert, G.S. and Rothmund, H., "Three-Dimensional Flow Over a Conical Afterbody Containing a Centred Propulsive Jet: A Numerical Simulation," AIAA Paper No. 83-1709, 1983.

13. Benek, J.A., Steger, J.L., Dougherty, F.C., and Buning, P.G., "A 3-D Chimera Grid Embedding Technique," AIAA Paper No. 85-1523, July 1985.

REFERENCES (Continued)

14. Belk, D.M. and Whitfield, D.L., "Three-Dimensional Euler Solutions on Blocked Grids Using an Implicit Two-Pass Algorithm," AIAA Paper No. 87-0450, January 1987.

15. Sahu, J. and Steger, J.L., "Numerical Simulation of Three Dimensional Transonic Flows," AIAA Paper No. 87-2293, August 1987.

16. Kayser, L.D. and Whiton, F., "Surface Pressure Measurements on a Boat-tailed Projectile Shape at Transonic Speeds," ARBRL-MR-03161, US Army Ballistic Research Laboratory, Aberdeen Proving Ground, Maryland, March 1982. (AD A113520)

17. Kline, R., Herrman, W.R., and Oskay, V., "A Determination of the Aerodynamic Coefficients of the 155mm, M549 Projectile," Technical Report 4764, Picatinny Arsenal, Dover, New Jersey, November 1974.

18. Whyte, R.H., Burnett, J.R., Hathaway, W.H., and Brown, E.F., "Analysis of Free Flight Aerodynamic Range Data of the 155mm M549 Projectile," ARLCD-CR-80023, US Army Large Caliber Weapon Systems Laboratory, Dover, New Jersey, October 1980.

19. Murphy, C.H., "Private Communications," US Army Ballistic Research Laboratory, Aberdeen Proving Ground, Maryland, September 1988.

20. Baldwin, B.S. and Lomax, H., "Thin Layer Approximation and Algebraic Model for Separated Turbulent Flows," AIAA Paper No. 78-257, 1978.

DISTRIBUTION LIST

No. of Copies	Organization	No. of Copies	Organization
12	Administrator Defense Technical Info Center ATTN: DTIC-DDA Cameron Station Alexandria, VA 22304-6145	1	Commander US Army Armament, Munitions and Chemical Command ATTN: SMCAR-ESP-L Rock Island, IL 61299-7300
1	HQDA (SARD-TR) Washington, DC 20310	1	Commander US Army Aviation Systems Command ATTN: AMSAV-DACL 4300 Goodfellow Blvd. St. Louis, MO 63120-1798
1	Commander US Army Materiel Command ATTN: AMCDRA-ST 5001 Eisenhower Avenue Alexandria, VA 22333-0001	1	Director US Army Aviation Research and Technology Activity Ames Research Center Moffett Field, CA 94035-1099
1	Commander US Army Laboratory Command ATTN: AMSLC-TD Adelphi, MD 20783-1145	1	Commander US Army Communications - Electronics Command ATTN: AMSEL-ED Fort Monmouth, NJ 07703-5301
1	Commander Armament R&D Center US Army AMCCOM ATTN: SMCAR-MSI Picatinny Arsenal, NJ 07806-5000	1	Commander US Army Missile Command ATTN: AMSMI-RD Redstone Arsenal, AL 35898-5000
1	Commander Armament R&D Center US Army AMCCOM ATTN: SMCAR-TDC Picatinny Arsenal, NJ 07806-5000	1	Commander US Army Missile Command ATTN: AMSMI-AS Redstone Arsenal, AL 35898-5000
2	Commander US Army Armament Research, Development and Engineering Center ATTN: SMCAR-LCA-F/Klein Hudgins Dover, NJ 07801-5001	1	Commander US Army Tank Automotive Command ATTN: AMSTA-DI Warren, MI 48090
1	Director Benet Weapons Laboratory Armament R&D Center US Army AMCCOM ATTN: SMCAR-LCB-TL Watervliet, NY 12189-4050	1	Director US Army TRADOC Analysis Center ATTN: ATAA-SL White Sands Missile Range, NM 88002-5502
		1	Commandant US Army Infantry School ATTN: ATSH-CD-CSO-OR Fort Benning, GA 31905-5400

DISTRIBUTION LIST

No. of Copies	Organization	No. of Copies	Organization
2	Commander US Naval Surface Weapons Center ATTN: Dr. T. Clare, Code DK20 Dr. F. Moore Dahlgren, VA 22448-5000	1	University of Maryland Department of Aerospace Engineering ATTN: Dr. J.D. Anderson, Jr. College Park, MD 20742
3	Director NASA Ames Research Center ATTN: MS-202-1/Pulliam MS-258-1/Steger Schiff Moffett Field, CA 94035	1	Florida Atlantic University Department of Mechanical Engr. ATTN: Prof. W. L. Chow Boca Raton, FL 33431
1	AFWL/SUL Kirtland AFB, NM 87117	1	University of Notre Dame Department of Aeronautical & Mechanical Engineering ATTN: Prof. T.J. Mueller Notre Dame, IN 46556
1	Air Force Armament Laboratory ATTN: AFATL/DLODL Eglin AFB, FL 32542-5000	1	University of Texas Department of Aerospace Engineering and Engineering Mechanics ATTN: Dr. D.S. Dolling Austin, Texas 78712-1055
2	Sandia National Laboratories ATTN: Dr. W.L. Oberkampf Dr. F. Blottner Division 1636 Albuquerque, NM 87185		**Aberdeen Proving Ground**
1	AEDC Calspan Field Services ATTN: MS 600 (Dr. John Benek) AAFS, TN 37389		Dir, USAMSAA ATTN: AMXSY-D AMXSY-MP, H. Cohen Cdr, USATECOM ATTN: AMSTE-TO-F
1	University of California, Davis Department of Mechanical Engr. ATTN: Prof. H.A. Dwyer Davis, CA 95616		Cdr, CRDC, AMCCOM ATTN: SMCCR-RSP-A SMCCR-MU SMCCR-SPS-IL
1	Pennsylvania State University Department of Aerospace Engr. ATTN: Dr. G. S. Dulikravich University Park, PA 16802		
1	University of Florida Dept. of Engineering Sciences College of Engineering ATTN: Prof. C. C. Hsu Gainesville, FL 32611		